Chapter 2
ZnO–Nanocarbons Core–Shell Hybrid Quantum Dots

2.1 ZnO–Graphene Quasi Core–Shell Hybrid Quantum Dots

2.1.1 Synthesis

Surface of graphite powder (Alfa Aesar, 5 g) was modified by ultrasonically by using 120 ml of a 1:3 mixture of HNO_3 (17 M) and H_2SO_4 (18 M) for 2 h at a power level of 200 W, while maintaining the temperature at 45 °C and functionalized oxygen-contained moieties such as epoxy (C–O–C), carboxyl (–COOH), and hydroxyl (–OH) etc. The dispersion was maintained at room temperature for 4 days, during which time the color of the dispersion became charcoal. The dispersion was then washed repeatedly with water in a cycle of centrifugation and decantation, and finally with ethanol. The product was allowed to dry at 55 °C for 12 h. The final graphite power with oxygen-based functional groups had a greyish appearance and was not as shiny as the starting material (Son et al. 2012a, b, c).

Mixed acids H_2SO_4 and HNO_3-treated graphite oxide (GO) power (40 mg) was uniformly dispersed in 40 ml of DMF ultrasonically for 10 min. Zinc acetate dihydrate [$Zn(CH_3COO)_2{\cdot}2H_2O$] (0.92 g) was dissolved in 200 ml of DMF, then the GO solution was added while continually stirring to form a stable precursor. Embryo ZnO quantum dots (QDs) were preferentially formulated in the early stage as a result of the chemical reaction through dehydration process as follows.

$$\begin{aligned} &Zn(CH_3COO)_2 \times H_2O + (CH_3)_2NC(O)H \\ &\quad \rightarrow ZnO + (CH_3COO)_2CHN(CH_3)_2 + H_2O \end{aligned}$$

And ZnO QDs uniformly grew up to the size of less than 10 nm in diameter as illustrated in Fig. 2.1.

W.K. Choi, *ZnO–Nanocarbon Core–Shell Type Hybrid Quantum Dots*,
Nanoscience and Nanotechnology, DOI 10.1007/978-981-10-0980-8_2

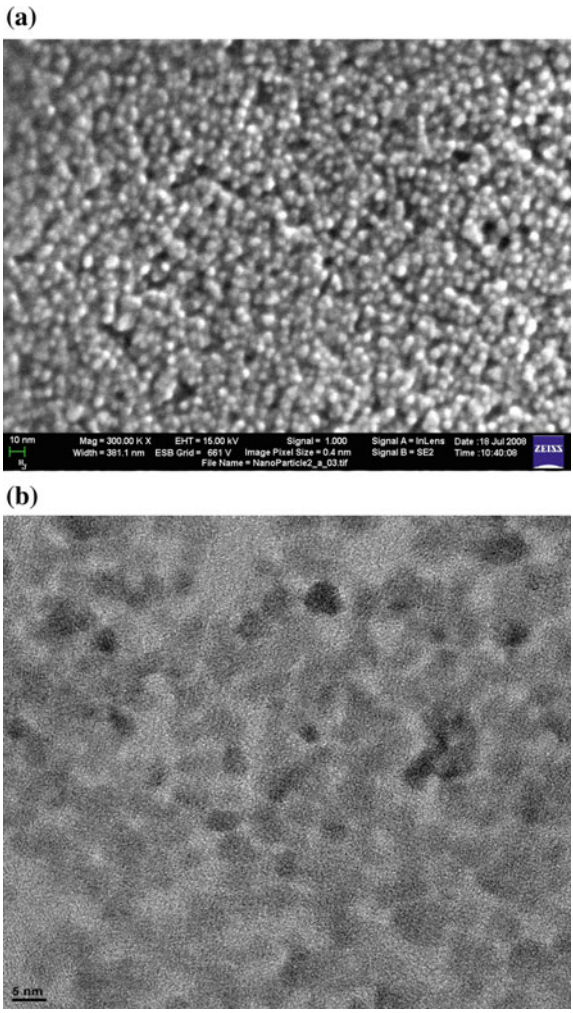

Fig. 2.1 **a** Scanning electron microscope image (×300,000) of **b** high resolution transmission electron microscope image of ZnO QDs

Subsequently, the mixed solution was heated to 95 °C and maintained at that temperature for 5 h. The color of the ZnO–graphene QDs then changed to white-greyish. This was subjected to repeated washing with ethanol by centrifugation, and finally with water. The final ZnO–graphene quantum-dot powder was obtained after drying the product at 55 °C as described in Fig. 2.2. In the formation of ZnO–graphene QDs, two chemical reaction are expected. One is chemical reaction between Zn^{2+} ions chemisorbed on the embryo ZnO QDs (denoted as Zn^{2+}(ZnO)) and the induced functional groups on the GO powder, leading to the local creation of new Zn–O–C bonding. Since ZnO is usually formed into oxygen-vacant nonstoichiometric oxide particles, Zn^{2+}(ZnO) ions exist dominantly on the surface of ZnO QDs and easily react with oxygen groups induced on the GO

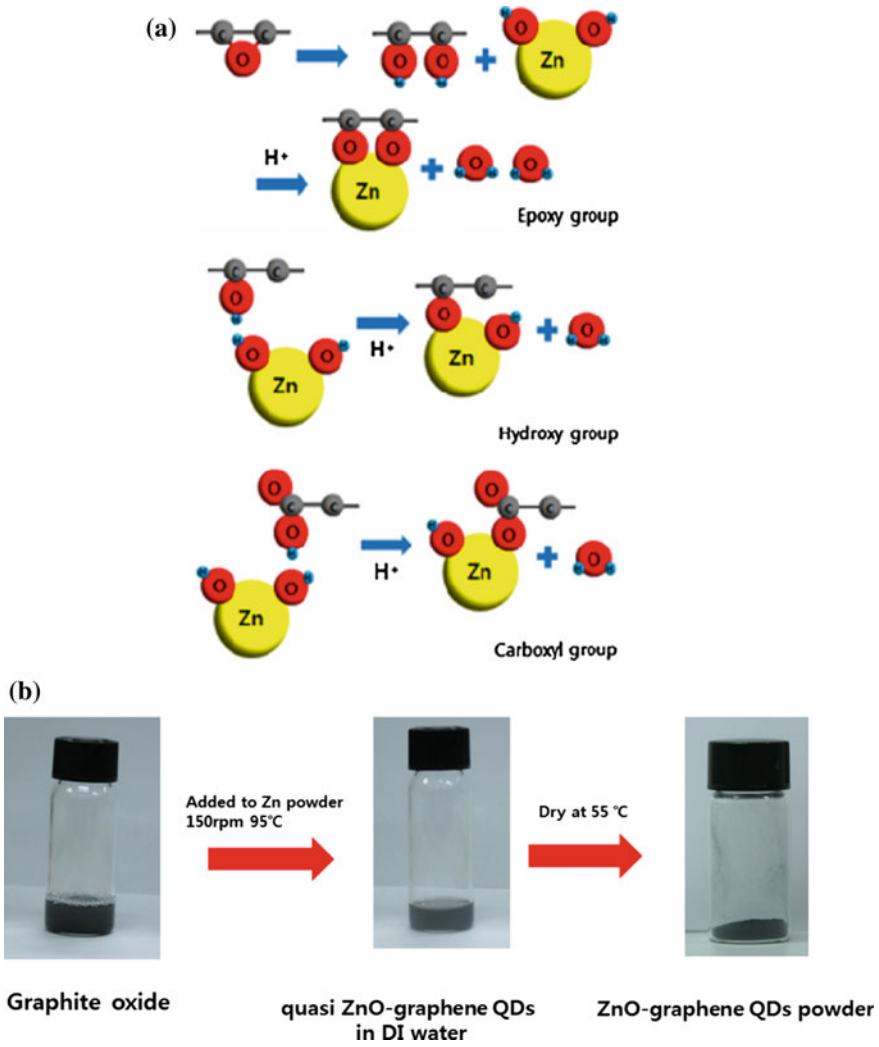

Fig. 2.2 **a** Chemical reaction model between Zn^{2+}(ZnO) and oxygen-based functional groups on the graphite oxide (GO) powder. **b** Chemical process of the preparation of ZnO–graphene QDs

powder surface in the DMF solution, where all three different reaction kinds of functional groups, epoxy, hydroxyl, and carbonyl with Zn^{2+}(ZnO) would produce the same Zn–O–C local bonding through similar dehydration process as shown in Fig. 2.3d.

In another reaction, Zn^{2+} ions bonded on the GO powder (denoted as Zn^{2+}(GO)) will react with O on ZnO QDs. During Zn–O–C bonding formation, the oxygen functionalities on the GO powder were almost reduced and a few layer graphene

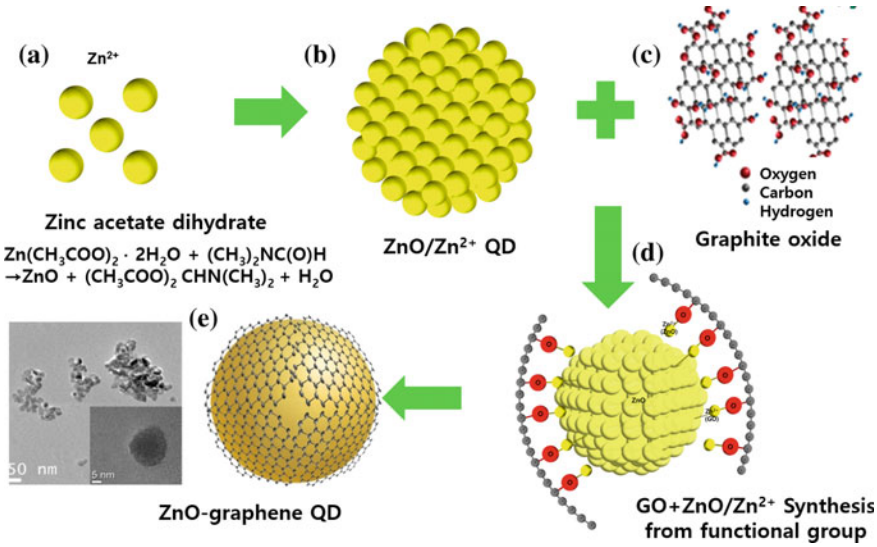

Fig. 2.3 Synthesis process for ZnO–graphene hybrid QDs. **a** Zn acetate dehydrate as a staring material to form ZnO NPs (**b**). **c** Chemical function group induced on graphite powder by acid treatment. **d** Synthesis of ZnO–graphene QDs through the formation Zn–O–C bonding between GO and Zn^{2+}. **e** Graphene QDs covered ZnO–graphene hybrid QDs and TEM image

quantum dots are detached from the GO powder via deoxidation, cutting process or a kind of chemical peel-off (i.e. chemical exfoliation) through the following reaction.

$$Zn(CH_3COO)_2 + 2H_2O \rightarrow Zn(OH)_2 + 2CH_3COOH$$
$$Zn(OH)_2 + \text{Carbon functional groups } (C{-}O{-}C,\ COOH,\ C=O) \rightarrow Zn{-}O{-}C + H_2O$$

In consequence, new functional nanoparticle of partially encircled ZnO–graphene consolidated hybrid quantum dots with quasi-core–shell structure can be synthesized. The whole synthetic model was conceptually depicted in Fig. 2.3. The chemical reaction of embryonic ZnO QDs with defect-like sites generated on GO powder surfaces plays a key role in stripping a monolayer or a few layer graphene quantum dot from the GO layers. The product of this reaction was then washed in water and dried to obtain pure ZnO–graphene quasi core–shell QDs.

2.1.2 Structural Characterization: XRD and TEM

Figure 2.4 shows the x-ray diffraction patterns for (a) pristine graphite powder, (b) GO powder treated without oxidant $KMnO_4$, and (c) that with $KMnO_4$ respectively. Main diffraction peak corresponding to G(002) from pristine graphite

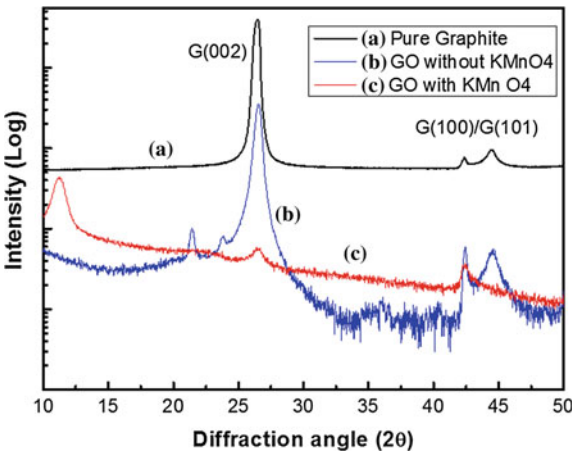

Fig. 2.4 X-ray diffraction patterns for pristine graphite powder, GO powder treated by mixed acids H_2SO_4 and HNO_3 with/without oxidant $KMnO_4$

powder was strongly observed at $2\theta = 26.48°$ and the other diffraction peaks from G(100) and G(101) were also detected at $2\theta = 42.36°$ and 44.44°. The GO powder treated without $KMnO_4$ showed similar XRD patterns to graphite powder without much change in diffraction peak intensity. This means that mixture of HNO_3 and H_2SO_4 without $KMnO_4$ less oxidized graphite powder and just moderately induced oxygen-based functional groups. When graphite powder was treated by $KMnO_4$ together, new diffraction peak around $2\theta = 11.26°$ was occurred and the peak corresponding to G(101) disappeared. The peak observed at the low angle near $2\theta = 10–12°$ is well known as fully oxidized graphite or graphene oxide (Son et al. 2012a, b, c). This revealed that $KMnO_4$ played an effective role for oxidizing graphite powder.

The HRTEM image of the ZnO–graphene quasi core–shell quantum dots is shown in Fig. 2.5a and clearly shows that the outer shell of the ZnO-core quantum dot looks like a single graphene layer. The enlarged view of the HRTEM image at the right bottom in Fig. 2.5b from the layer encircling by yellow color reveals that the interplanar spacing in the crystalline petal is 0.26 nm, which corresponds to the distance between two (002) planes of the hexagonal ZnO phase, indicating preferential growth along the [002] direction (c-axis). From another HRTEM analysis, close inspection of the dark areas in each of the images taken from the layer encircling the ZnO quantum dots by red color suggests that the layer is monolayer graphene, because a hexagonal atomic lattice with uniform contrast from the enlarged white color square region can be clearly discerned and the measured distance between carbon atoms of 0.14 nm agrees well with the theoretical value for graphene.

In Fig. 2.6, x-ray diffraction (XRD) patterns for the ZnO QDs, the ZnO–graphene quasi core–shell quantum dots, graphene sheets, and graphite powder are illustrated. For ZnO QDs, ZnO Bragg peaks (100), (002), (101) and (102) can be seen; the positions and intensity ratios of these peaks agree well with those of standard ZnO bulk (JCPDS no. 36-1451) and thus ZnO QDs were believed as being

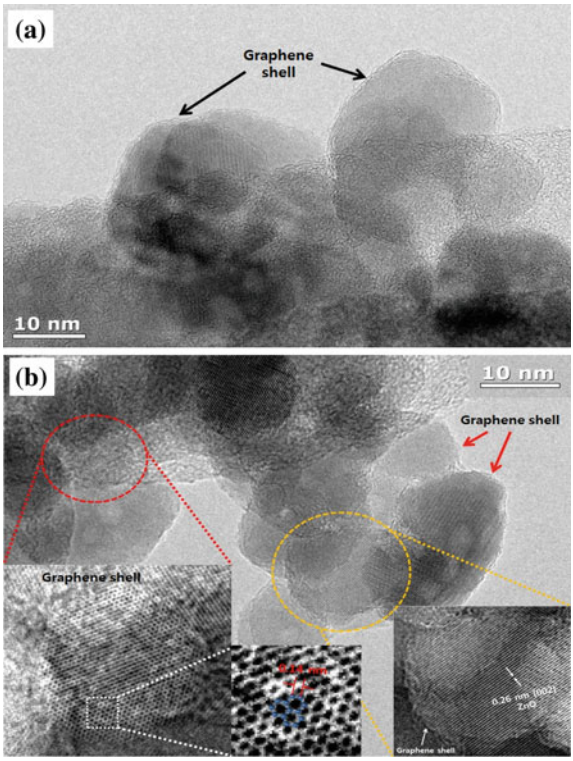

Fig. 2.5 HR-TEM images for ZnO–graphene core–shell hybrid quantum dots. **a** Outer *black line* indicates graphene shells. **b** Enlarged picture of both white rectangular and *yellow circle* regions represents typical graphene hexagons and ZnO NPs

polycrystalline phase. For the ZnO–graphene quasi core–shell quantum dots, Bragg peaks corresponding to both ZnO and graphene are observed simultaneously, indicating that the consolidated ZnO–graphene quasi-core–shell quantum dots have been successfully synthesized from GO powder and zinc acetate dihydrate powder. The appearance of both a broad intense G (002) peak centered at $2\theta \approx 25.8°$ (d = 0.34 nm, with a large full-width at half-maximum (FWHM) as great as 2.34°) and a very broad peak denoted as G (100) at $2\theta = 43.5°$ with low intensity are strong evidence supporting for the existence of the graphene layer on the ZnO quantum dots. For comparison, XRD from graphite powder and graphene sheet are also added. XRD for graphite powder is the same with that aforementioned in Fig. 2.4. Graphene sheet is obtained by dissolving core ZnO QDs using HCl acid which will be discussed in Application section and is a kind of agglomerated graphene QDs chemically adsorbed on the inner ZnO. The diffraction peak form graphene sheet is happened at around $2\theta = 26°$ and shows relatively small intensity compared to that of graphite powder.

Figure 2.7a represents HRTEM images of ZnO–graphene QDs and enlarged images of white circle area (scanning line is depicted as white dot line in the right picture) Corresponding the energy dispersive x-ray spectroscopy (EDX) image of ZnO–graphene QDs was obtained by line scanning along the red line represented in

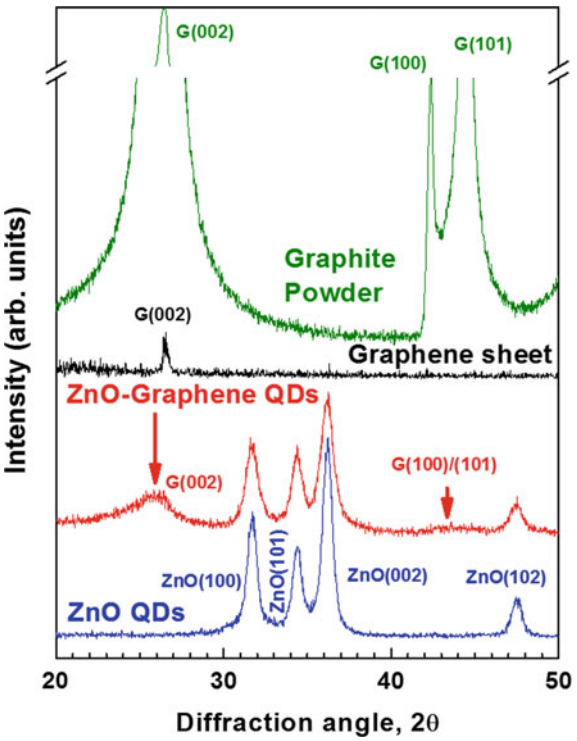

Fig. 2.6 X-ray diffraction patterns for the ZnO QDs, the ZnO–graphene quasi core–shell quantum dots, graphene sheets, and graphite powder

the left picture of Fig. 2.7b. In the right picture of Fig. 2.7b, peak intensity of C gradually increased at the edge but a little decreased at the center and reincreased after passing over the center. But those intensity of O and Zn showed the maximum at the center and symmetrically decreased at the edges. These results well support the existence of graphene layer outside ZnO core in ZnO–graphene QDs. From Thin Film Standardless Standard Quantitative Analysis (Fitting Coefficient: 0.6759) based on elemental x-ray emission peak of C K_α(0.277 keV) as reference, O K_α (0.525 keV), and Zn K_α (8.630 eV), atomic percentage was estimated as C (91.61 %):O(2.44 %):Zn(5.96 %), and corresponding compound as C(1):O(0.42): Zn(0.51) respectively (Fig. 2.7c).

In addition, a HR-HAADF (high resolution high angle annular dark field) STEM (scanning transmission electron spectroscopy) image (Fig. 2.8a) combined with an Energy Dispersive Spectrometry (EDS) image scanned across a single ZnO–graphene quasi core–shell QD were obtained. Figure 2.8b, d exhibit the drift corrected spectrum profile scanning EDS data of the C K line, O K line, and Zn L line of the ZnO–graphene quasi core–shell QDs, respectively. As seen in Fig. 2.8c, d, the intensities of both the O K and Zn L lines appear to show a sudden increase near 5 nm and the values are remain steady and then decrease after passing a position at near 20 nm. For the C K line spectrum (Fig. 2.8b), the intensity appears to increase after passing the position near 5 nm and then remains at a constant value.

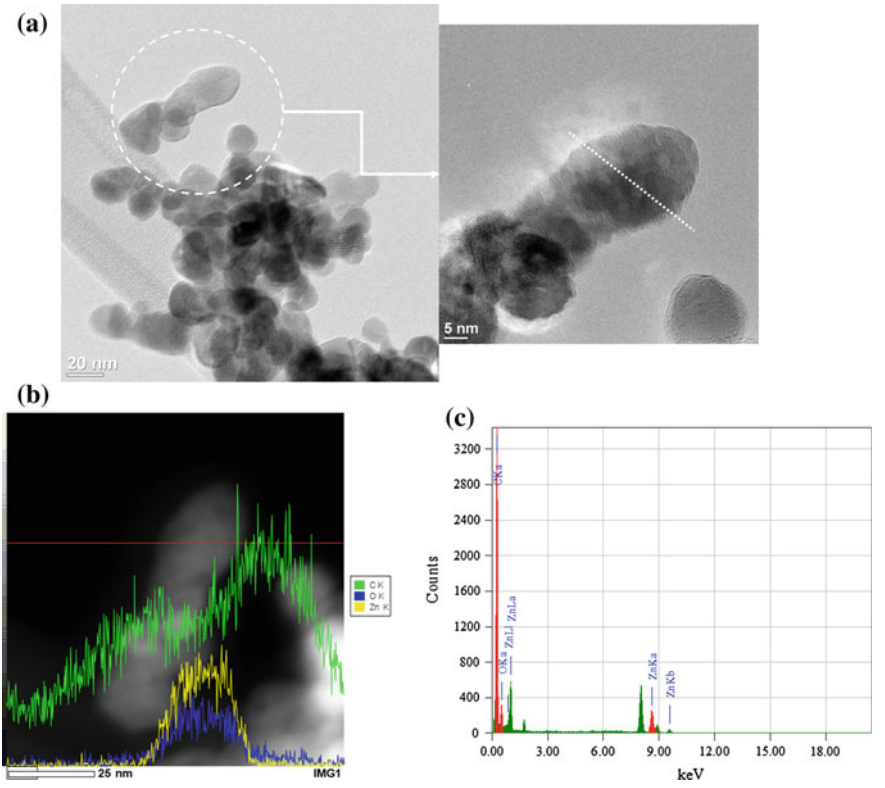

Fig. 2.7 TEM images of **a** ZnO–graphene core–shell hybrid QDs. **b** Scanned EDX profile corresponding to C K_α, O K_α, and Zn K_α along the red line and **c** EDX intensity

The increasing intensity, even after passing near 20 nm, might result from the overlap with the bottom edge of the particle. Both the HR-HAADF and scanned EDS data unambiguously show that the synthesized ZnO–graphene QDs are quasi consolidated structures of the ZnO QDs surrounded by a graphene layer.

2.1.3 Composition Analysis by X-Ray Photoelectron Spectroscopy

Figure 2.9 illustrates x-ray photoelectron spectroscopy data for mixed acids H_2SO_4 and HNO_3-treated graphite oxide (GO) power with and without strong oxidant $KMnO_4$ for comparison. By deconvolution of the C1s and O1s core level peaks into subpeaks, relative amounts of oxygen-related functional groups and the ratio of C/O were calculated (Son et al. 2012a, b, c).

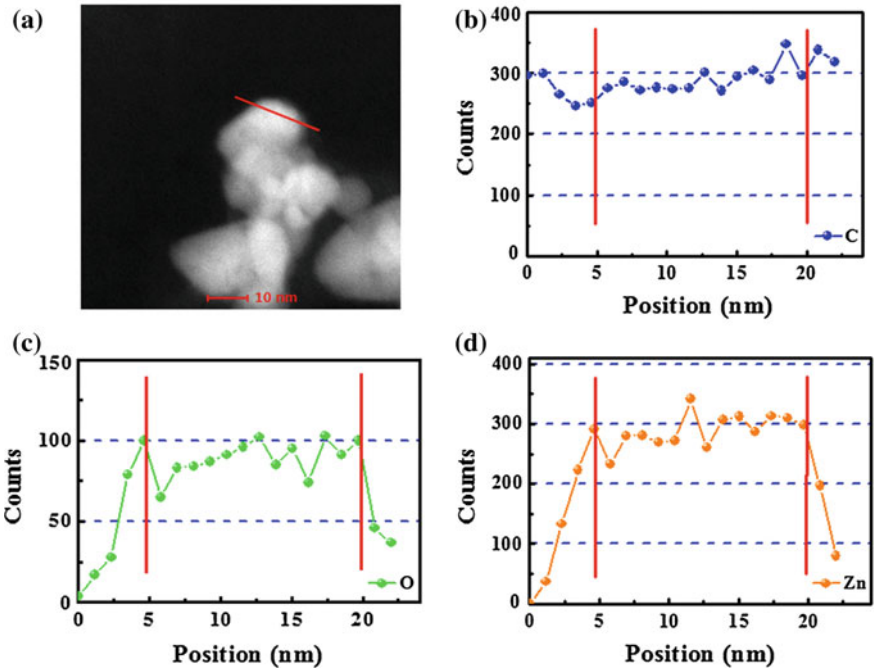

Fig. 2.8 HAADF STEM image **a** and spectrum profile scanning EDS of the C K_α line (**b**), O K_α line (**c**), and Zn L_α line (**d**) of ZnO–graphene quasi core–shell QDs (Reproduced from Son et al. 2012a, b, c)

Table 2.1 shows the amounts of carbon and oxygen, and the relative ratio C/O (XPS). The spectra were fitted after subtracting the Shirley background using the XPS Multipack Spectrum program. As presented in Table 2.1, the GO without addition of $KMnO_4$ showed the high C/O ratio of $\sim$10, but that treated with $KMnO_4$ showed small as much as $\sim$2 by large incorporation of oxygen contents. Even though the value of C/O of 10.07 is a little smaller than the value of 15.27 reported for RG-OHI-AcOH (Wang et al. 2008a, b) and 11.0 for highly reduced G–O (Moon et al. 2010), but was higher than the values of 9.97 (Cote et al. 2009) and 8.57 (Park et al. 2009) reported for chemically converted graphene.

On the other hand the value of 2.06 is close to the values of 1.4–1.7 reported for chemically exfoliated and highly oxidized graphene oxide nanoribbons obtained under various conditions using $KMnO_4$ (Li et al. 2008; Higginbotham et al. 2010), and similar to that of 2.5 for pristine graphene oxide obtained using similar chemical processes (Lomeda et al. 2008; Yang et al. 2009), and 2.1 using the modified Hummers method (Fan et al. 2011). The C1s signals were deconvoluted into sp2 C (284.5–284.6 eV), sp3 C (285.5–285.6 eV), C–O (286.1–286.7 eV), C=O (287.5–287.8 eV), –COO– (288.8–289.2 eV), and a π–π^* satellite peak (290.6 eV) (Fan et al. 2011; Mattevi et al. 2009). From the XPS result, it can be

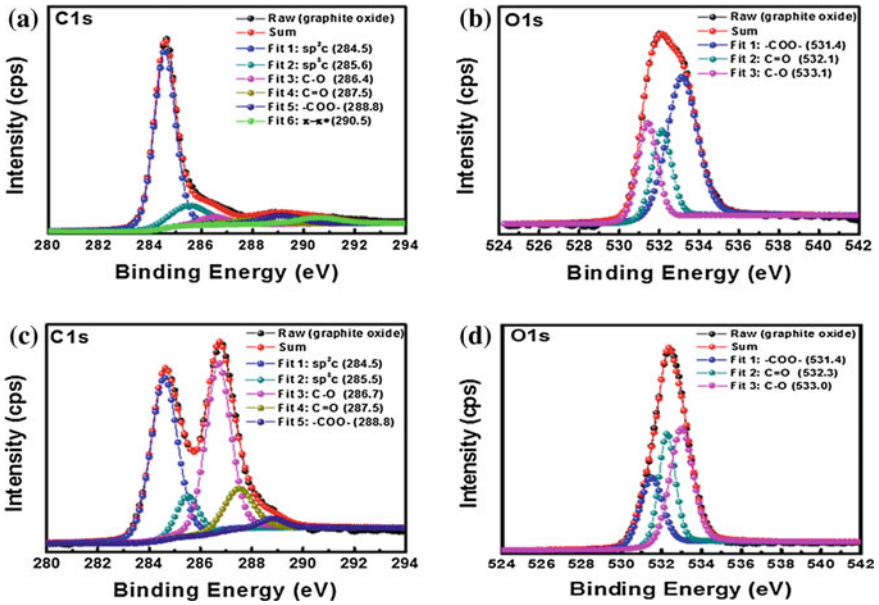

Fig. 2.9 XPS C1s (**a**) and O1s (**b**) core-level spectra for the GO treated with mixture H_2SO_4 and HNO_3 without $KMnO_4$ and C1s(**c**) and O1s (**d**) for the GO treated with mixture H_2SO_4 and HNO_3 and $KMnO_4$ (Reproduced from Son et al. 2012a, b, c)

Table 2.1 C and O contents and relative C/O ratio obtained from the XPS (Fig. 2.9) for the GO powder treated H_2SO_4 and HNO_3 with/without $KMnO_4$

Materials	C (%)	O (%)	C/O
Pristine graphite power	99.03	0.97	102
GO without $KMnO_4$	90.97	9.03	10.07
GO with $KMnO_4$	67.06	32.43	2.06

Reproduced from Son et al. (2012a, b, c)

concluded that mixed acids H_2SO_4 and HNO_3-treated graphite oxide (GO) power were not highly oxidized, but a certain intercalated graphite powder with sulfate or nitrate ions, similar to a graphite intercalation compound (GIC) (Tang et al. 2009; Nakajima et al. 1988).

2.1.4 Raman Spectroscopy

Figure 2.10a presents the Raman spectra of the ZnO–graphene quantum dots. The G and D modes are known to arise from first order scattering of the E_{2g} phonon of sp2 carbon atoms and from a breathing mode of k-point photons of A_{1g}

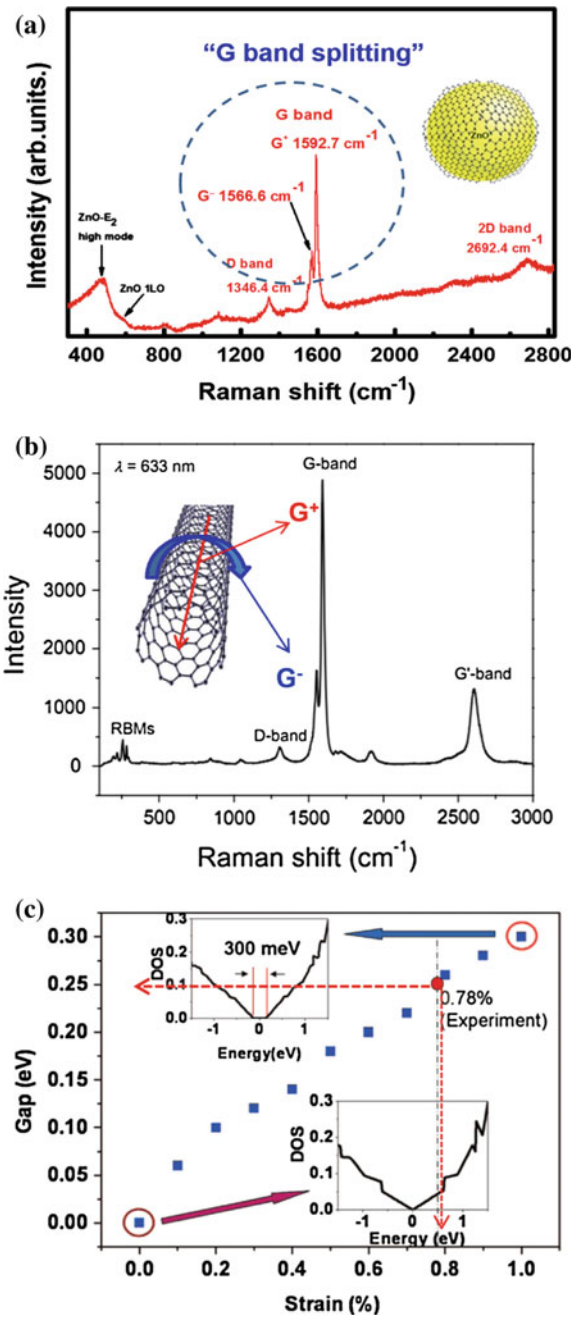

Fig. 2.10 Raman spectra for **a** ZnO–graphene core–shell hybrid QDs (Son et al. 2012a, b, c) and **b** single wall CNT. **c** Linear dependence of magnitude of bandgap opening of graphene on the strength of the applied uniaxial strain (Reproduced from Ni et al. 2008)

symmetry, respectively (Kudin et al. 2008). It is noteworthy that the doubly degenerate G peak splits into two sub-bands, namely G^+ (1592.7 cm^{-1}) and G2 (1566.6 cm^{-1}) (Mohiuddin et al. 2009), but this did not happen for the 2D peak. This splitting of the G band into two distinct sub-bands (G^+, G^-) results from strain induced symmetry breaking, with polarization along the strain as well as perpendicular to it, and the splitting increases with increasing strain. Such results are frequently observed in Raman spectra of single-walled CNT(SW CNT) as shown in Fig. 2.10b. The G band splitting becomes less pronounced as the CNT diameter increases and disappears for large CNT radii or for the case of multi-walled CNTs (Rodriguez et al. 2012). This phenomenon can be explained well in terms of strain induced by bending of the graphene surrounding the ZnO quantum dots. Even though, in reality, the strain is not uniaxial, the applied strain can be approximated from the splitting of 26.1 cm^{-1} as $\varepsilon = 0.8$ %, calculated from the best linear fit of the variations of the positions of G^+ and G^- as a function of applied uniaxial strain, $\partial\omega_{G+}/\partial\varepsilon \approx -10.8\ cm^{-1}/\%$ and $\partial\omega_{G-}/\partial\varepsilon \approx -31.7\ cm^{-1}/\%$, provided uniaxial strain is applied. According to Ni et al. (2008), the magnitude of bandgap opening ($\Delta\varepsilon_g$) of graphene depends linearly on the strength of the applied uniaxial strain (as presented in Fig. 2.10c), and the induced strain of $\varepsilon = 0.8$ % applied here is equivalent to a bandgap opening of $\Delta\varepsilon_g \approx 250$ meV. Furthermore, the position of the sharp 2D peak at $\sim$2692.4 cm^{-1} is further evidence that the graphene covering the ZnO quantum dots is a monolayer, because a single layer of graphene has a single sharp 2D peak below 2700 cm^{-1} (Dato et al. 2008).

2.1.5 Time-Resolved Photoluminescence

Figure 2.11 shows PL spectra at room temperature for the ZnO graphene quantum dots, poly-TPD and pure ZnO quantum dots respectively. The PL peaks for the pure ZnO quantum dots and poly-TPD are observed at wavelengths of 379 nm (3.26 eV) and 460 nm (2.69 eV), which well corresponds to the known values of excitonic emission with a bandgap (Anikeeva et al. 2003; Son et al. 2009). In the PL of the ZnO–graphene quantum dots, two additional emissions peaking at 406 nm (3.05 eV) and 432 nm (2.86 eV) can be observed, with the difference of peak positions apart from those of the pure ZnO quantum dots as much as $\sim$190 meV. The conjugation of the graphene to the ZnO QDs leads to large extent of ca. 70 % of quenching of the UV PL emission with the appearance of new graphene peaks. The QD PL quenching effect may result from four different mechanism (Wang et al. 2008a, b). In this study, it can be presumed that the ZnO QD quenching in the presence of graphene is primarily caused by both the static quenching and charge transfer reactions. Unlike dynamic quenching, static quenching occurs when the donor and acceptor materials are in the ground state. Here, the inner ZnO QD is the donor and the graphene nanoshells are the acceptor. A possible quenching method is the fast deactivation of the excited state through the electron transfer reactions

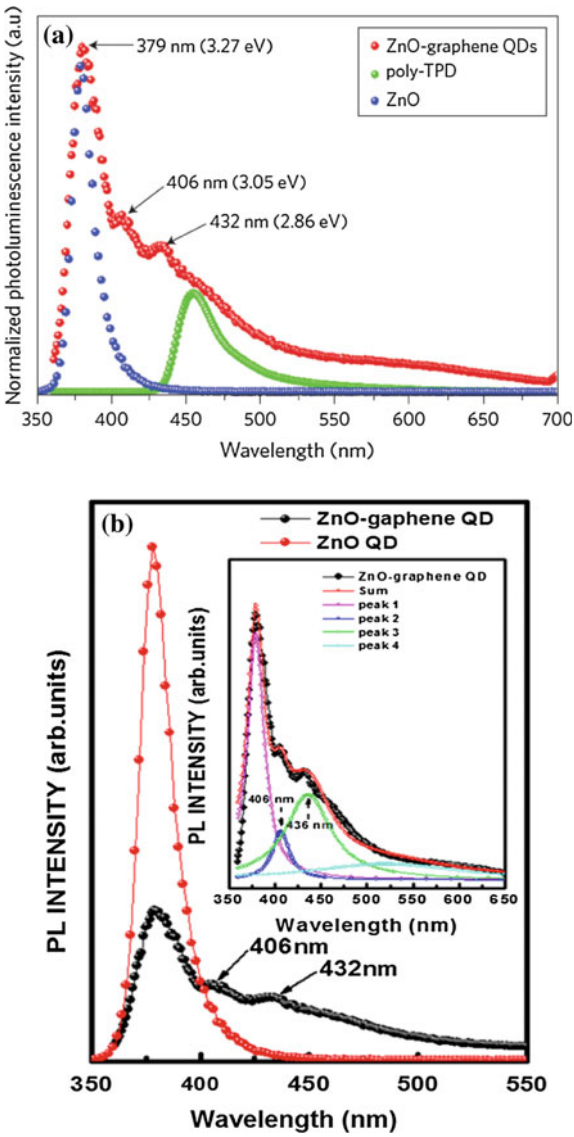

Fig. 2.11 **a** Photoluminescence spectra with normalized intensity for ZnO quantum dots, ploy-TPD, and ZnO–graphene quantum dots. **b** PL peak fitting with three subpeaks centered at 379, 406 and 436 nm (Reproduced from Son et al. 2012a, b, c)

from the conduction band of the ZnO to the lowest unoccupied molecular orbitals (LUMO) of the graphene quantum dots attached outside ZnO inner cores.

Qualitatively, this implies a high charge generation efficiency (Kumar et al. 2006). The three functional groups (carboxyl (–COOH), hydroxy (–OH), and

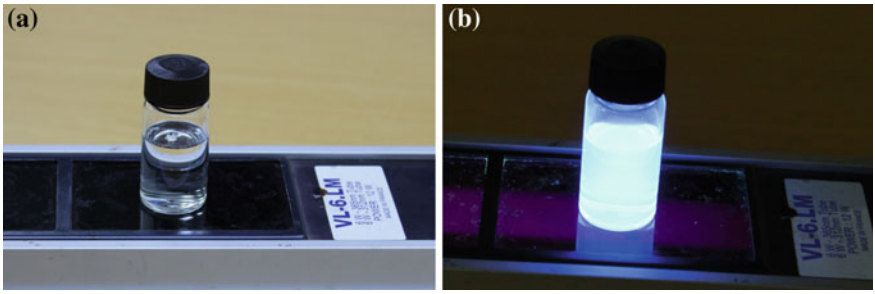

Fig. 2.12 Photographic images of transparent ZnO–graphene hybrid quantum dots solution dissolved in ethanol before (**a**) and after (**b**) irradiation of UV light (λ = 365 nm)

epoxy) formed on the GO surface can easily bind to the ZnO surface while forming the consolidated quasi core–shell QDs (which is confirmed in the subsequent analysis using XPS), resulting in strong PL quenching. Thus, the static quenching (strong quenching) of the QDs is caused by the three functional groups when it is attached to the ZnO surface and will be discussed further in the analysis of the time-resolved PL measurements.

Figure 2.12 is the photographic images of ZnO–graphene hybrid quantum dots dissolved in ethanol before (a) and after (b) exposure to UV light source (λ = 365 nm). As shown in Fig. 2.12a, ZnO–graphene quantum dots solution are transparent which means that they are well dispersed in ethanol without agglomeration. When this solution is exposed to UV light ((λ = 365 nm), very bright blue emission is observed as shown in Fig. 2.12b. This result strongly supports new blue emission observed in PL from ZnO–graphene hybrid quantum dots.

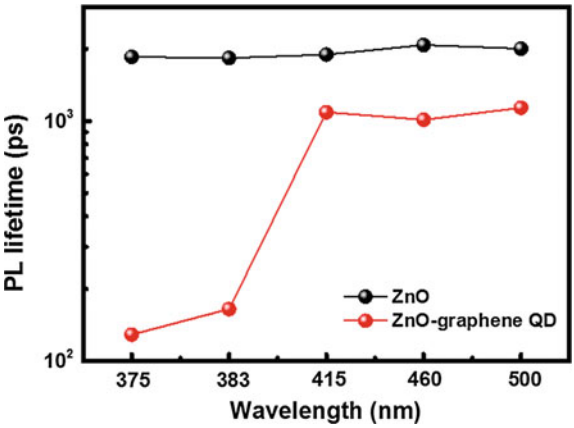

Fig. 2.13 The temporal evolution of the PL intensities taken by TRPL for the hybrid ZnO–graphene nanoshell QDs and for the ZnO QDs reference samples at 375, 383, 415, 460, and 500 nm (Reproduced from Son et al. 2012a, b, c)

Table 2.2 Exciton lifetimes (τ_{avr}) of ZnO QDs and ZnO–graphene core–shell QDs

Samples	Monitored wavelength, nm	τ_1 (f_1), ns	τ_2 (f_2), ns	χ^2	τ_{avr}, ns
ZnO	375	3.56 (0.44)	0.53 (0.56)	1.34	1.85
ZnO	383	3.52 (0.44)	0.50 (0.56)	1.27	1.83
ZnO–graphene	375	1.25 (0.04)	0.08 (0.96)	1.073	0.13
ZnO–graphene	383	1.31 (0.07)	0.08 (0.93)	1.12	0.17

Reproduced from Son et al. (2012a, b, c)

Time-resolved PL measurements for both the ZnO–graphene quasi QD and the ZnO QD reference sample were performed in order to consider the charge transfer between the ZnO QDs and the graphene nanoshells. Figure 2.13 presents the temporal evolution of the PL intensities for the hybrid ZnO–graphene nanoshell QDs and for the ZnO QDs reference samples at 375, 383, 415, 460, and 500 nm, measured using a time-correlated single photon counting setup. The PL lifetimes of the nanocomposite decreased significantly in comparison with those of the reference ZnO QDs without conjugation to the graphene nanoshells. Table 2.2 shows the fitting curves of the PL decay with a biexponential function to calculate the lifetime in the UV range (375 and 383 nm). The amplitude weighted average exciton lifetime (τ_{avr}) was $f_1\tau_1 + f_2\tau_2$, where f_1 and f_2 are fractional intensities and τ_1 and τ_2 are lifetimes. χ^2 is the reduced chi-square. The lifetimes (τ) of the hybrid ZnO–graphene nanoshell QDs and the reference ZnO QDs at various wavelengths were fitted using a second-order equation and are plotted in Fig. 2.13. Considering that the decays are biexponential in nature, the amplitude-weighted average lifetimes were estimated. The calculated average lifetimes of the 375, 383, 415, 460, and 500 nm states for the ZnO QD and the ZnO–graphene QD were (1852, 129 ps), (1832, 165 ps), (1893, 1088 ps), (2077, 1012 ps), and (2004, 1136 ps), respectively. The decay of the hybrid ZnO–graphene nanoshell QDs at all selected wavelengths was much faster than that for the reference sample of ZnO QDs, and this is indicative of the existence of an additional high efficiency relaxation channel in the former, which is believed to be a charge transfer from the ZnO QD to graphene nanoshells.

2.1.6 Density of States (DOS) Calculated by Density Functional Theory (DFT)

A simple model with density functional theory (DFT) as implemented in the Gaussian package (Frisch et al. 2004) for calculation of density of states (DOS) and projected density of states (PDOS) was adopted to give details for the occurrence of the two new peaks in the PL spectra. The local structures of graphene were simulated with several oxygen bonding with 19 aromatic rings. The oxygen

arrangement was achieved through several bond geometries, such as epoxy bonds and hydroxyl bonds in the basal plane and carboxyl groups at the edge, and the three cases were calculated. A Becke-style three-parameter Lee-Yang-Parr hybrid functional with a split basis set of 6-31G* was implemented to make calculations. A large periodic graphene model was not generated because this size of local model quite sufficiently to excerpt the core properties of the energy level changes associated with oxygen bonding geometries. First, a pristine structure with a planar geometry was generated to represent the graphene. Then, an oxygen atom with several bond types was attached as a model for the graphene–oxygen (G–O) bridging ZnO QD and the geometry fully relaxed to meet minimum energy requirements. Four different G–O models were selected and the DOS, PDOS, and molecular orbital characters were sequentially calculated for each G–O. The molecular structures of fully relaxed G–Os are depicted in Fig. 2.14a, e.

Figure 2.14f shows the calculated DOS of the graphene models. The magnified (5×) PDOS of oxygen is indicated with the blue line and the Kohn–Sham molecular orbital energy is indicated by the vertical bars. Comparing the pristine graphene with the other G–Os, a perceptible change is observed in the LUMO region. The oxygen attachments induce significant orbital hybridization between the oxygen orbital and the *p* orbital of the pristine graphene; thus, the LUMO level of the pristine graphene splits (vertical arrows) into 2, 3 or 4 molecular orbitals. The oxygen PDOS clearly shows a contribution to the newly emerging levels; therefore, these levels are directly related to the oxygen attachment. These emergent energy levels could alter the orbital character of the pristine graphene. The PL process in the ZnO QD can also occur via another route: the oxygen atom connects the ZnO QD with the graphene and the photoexcited electrons from the valence band (O 2*p*) of the ZnO QD are transferred to the unoccupied states of the G–Os. Then, these electrons undergo transition down to the original O 2*p* ground state leading to the PL emission. However, because the transition is satisfied by the selection rule ($\Delta l = \pm 1$), only electrons with *s* ($l = 0$) or *d* ($l = 2$) characteristics are allowed to transit to the O 2*p* ($l = 1$) level of the ZnO QDs. For pristine graphene, the LUMO level consists of the *p* orbitals of the aromatic rings; thus, the transition is prohibited during the PL process ($\Delta l = 0$). However, the newly emerged levels in the G–O having *s* orbital characteristics are occurred and the electrons in these levels can transit to the O 2*p* of ZnO QDs ($\Delta l = 1$). This corresponds well with the two newly emerged features in the PL spectra (406 and 432 nm) as shown in Fig. 2.11.

In order to quantify which oxygen bonding predominantly determines the PL transition, the percentage contributions of *s* and *p* orbitals to LUMO, LUMO+1, and LUMO+2 of the G–Os were evaluated. For Fig. 2.14b basal epoxy, LUMO and LUMO+2 have a definite contribution from *s* orbital (7.1 and 6.7 %, respectively; red arrows), while LUMO+1 (black arrow) has a negligible *s* orbital character. Meanwhile, for the 14(c) basal center, the LUMO has a significant *s* orbital character (19 %; red arrow) and its energetic position is identical to the LUMO of Fig. 2.14b basal epoxy. These levels have the three largest *s* characters among the levels in four different G–Os; thus, these three levels play a crucial role in the new features of the PL emission. Therefore, the photoexcited electron from the ZnO QD

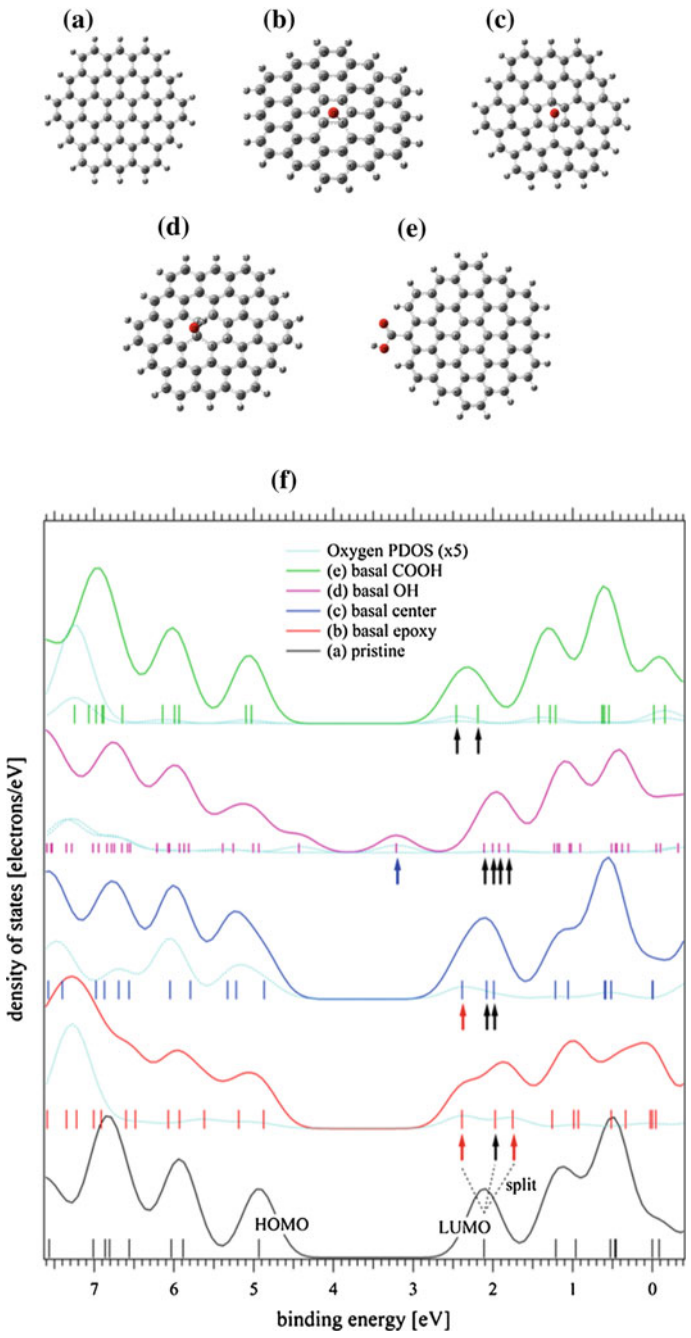

Fig. 2.14 Optimized structure of **a** pristine, **b** basal epoxy, **c** basal center, **d** basal –OH and **e** edge –COOH graphene model with 19 aromatic rings. **f** Calculated density of states (DOS) and oxygen projected DOS. LUMO splits are also depicted with *vertical arrows* (Reproduced from Son et al. 2012a, b, c)

can have a ground state transition using these new levels in the graphene shell, and it corresponds to the two new features in the PL spectrum, with the two levels being energetically identical.

Although the energetic distance between the newly emerged levels in the DFT results is larger than that of the PL emission, this does not significantly interfere with the underlying physics because the discrepancy is only a systematic error from the inherent properties of DFT, such as the energy gap underestimation. For Fig. 2.14d basal OH, only the LUMO (blue arrow) level has a definite *s* orbital contribution (5.8 %) and the other frontier levels have a negligible *s* character (<1 %). However, Fig. 2.14d basal OH is not found in the G–Os, as shown in the XPS core level spectra (Fig. 2.9). In addition, compared with the PL features, the energetic difference between the LUMO of Fig. 2.14d basal OH and the other levels of Fig. 2.14b basal epoxy and Fig. 2.14c basal center are too large. Therefore, Fig. 2.14d basal OH–graphene is not a dominant bridging structure of the ZnO–graphene core–shell. Interestingly, Fig. 2.14e edge COOH splits the pristine LUMO into two levels without *s* hybridization occurring. Therefore, the LUMO and LUMO+1 of Fig. 2.14e edge COOH do not contribute to the PL emission. Collectively, the new PL features originate primarily from the LUMO and LUMO +2 of Fig. 2.14b basal epoxy and the LUMO of Fig. 2.14c basal center, which bridge the ZnO QD to graphene (Son et al. 2012a, b, c).

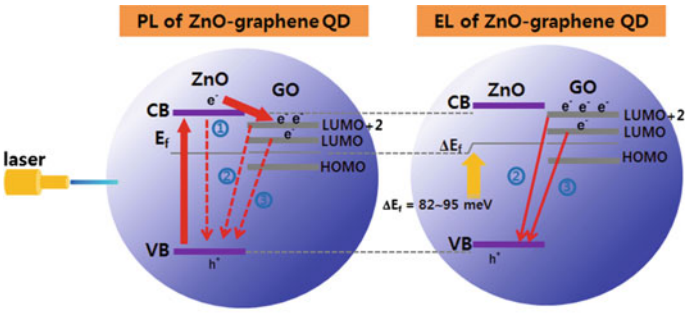

	Transition	PL	EL
1	$CB_{ZnO} \rightarrow VB_{ZnO}$	379 nm: (3.27 eV)	×
2	$LUMO_{GO} \rightarrow VB_{ZnO}$	406 nm: (3.05 eV)	428 nm: (2.89 eV)
3	$LUMO+2_{GO} \rightarrow VB_{ZnO}$	432 nm: (2.86 eV)	452 nm: (2.74 eV)

Fig. 2.15 Photoluminescence and electroluminescence transition scheme for ZnO–graphene quasi-quantum dots. Transitions 1, 2 and 3 correspond to electron transitions from the conduction band (CB) of ZnO, LUMO+2 and LUMO levels induced by G–O_{epoxy} to the valence band (VB) of ZnO, respectively (Reproduced from Son et al. 2012a, b, c)

Table 2.3 Percentage contribution of *s* and *p* orbitals to LUMO, LUMO+1 and LUMO+2 of four different kinds of graphene–oxygen (G–O) bonds

Ligand		*s* orbital contribution (%)	*p* orbital contribution (%)
Epoxy (–O)	LUMO (2.39 eV)	7.1	92.4
	LUMO+1 (1.97 eV)	0.6	99.1
	LUMO+2 (1.75 eV)	6.7	92.8
Centered epoxy (–O)	LUMO (2.39 eV)	19.4	80.2
	LUMO+1 (2.08 eV)	2.0	97.6
	LUMO+2 (1.99 eV)	2.3	97.2
Hydroxy (–OH)	LUMO(β) (3.21 eV)	5.8	93.7
	LUMO(α) (2.11 eV)	0.2	99.5
	LUMO+1 (β) (2.00 eV)	0.2	99.4
	LUMO+1 (α) (1.92 eV)	2.2	97.4
	LUMO+2 (β) (1.81 eV)	2.7	96.9
Carboxyl (–COOH)	LUMO (2.46 eV)	0.0	100.0
	LUMO+1 (2.19 eV)	0.0	100.0

Reproduced from Son et al. (2012a, b, c)

Figure 2.15 illustrates the schematic PL process from ZnO–graphene hybrid QDs electronic transition and EL process occurred in ZnO–graphene QDs based device. Electronic transitions from (LUMO+2)G–O_{epoxy} or (LUMO)G–O_{epoxy} to VB_{ZnO} correspond to two PL peaks of 406 nm (3.05 eV) and 436 nm (2.84 eV) respectively and also correlate with two EL of 428 nm (2.89 eV) and 452 nm (2.74 eV) respectively (Table 2.3).

2.2 ZnO–C_{60} Hybrid Quantum Dots

2.2.1 Synthesis

In a similar way as described in Sect. 2.1.1, C_{60} oxide was prepared by treating C_{60} natural powder with a mixed acid of H_2SO_4 and HNO_3 was treated and; thus, three functional groups, carboxyl (–COOH), hydroxy (–OH), and epoxy, could be induced on the C_{60} surface. Thereafter, in the mixture of Zn acetate dihydrate with C_{60} oxide in DMF solution, embryo ZnO QDs were preferentially formed in the early stages under the chemical reaction $Zn(CH_3COO)_2{\cdot}H_2O + (CH_3)_2NC(O)H \rightarrow ZnO + (CH_3COO)_2{\cdot}CHN(CH_3)_2 + H_2O$ and grew up to the size of about 5 nm in diameter. Then, at the outmost edge of the embryo ZnO QDs, two chemical reactions most likely occurred as shown in Fig. 2.16b. In one reaction, Zn^{2+} ions, denoted as Zn^{2+}(ZnO), chemisorbed on embryo ZnO QDs, react with functional groups on C_{60} and as a result, creates local Zn–O–carbon bonding. In another

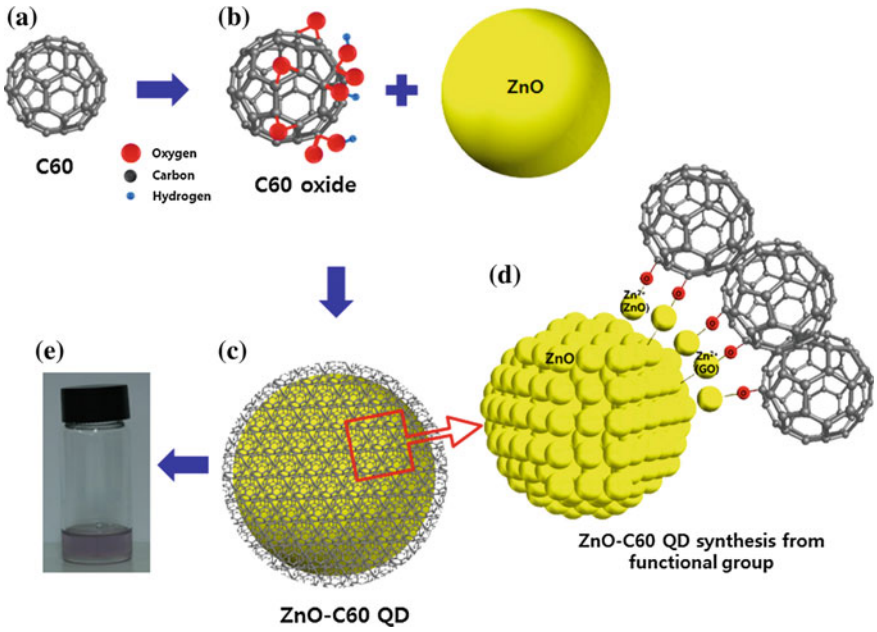

Fig. 2.16 The schematics of conceptual chemical synthesis of ZnO–C_{60} core–shell QDs. **a** Induced functional groups on the C_{60} oxide surface after treatment with an acid of H_2SO_4: HNO_3 = 3:1. **b** Embryo ZnO QDs formed under the chemical reaction and formation of the ZnO–C_{60} core–shell QDs. **c** Schematics of the ZnO–C_{60} core–shell QDs. **d** The possible chemical reactions between three kinds of functional groups (carboxyl (–COOH), hydroxy (–OH), and epoxy) and C_{60} oxide. **e** Image of the ZnO–C_{60} QDs in DMF solution (Reproduced from Son et al. 2012a, b, c)

reaction, Zn^{2+} ions ($Zn^{2+}(C_{60})$) bonded onto C_{60} also form Zn–O bonding and then combined with embryo ZnO QDs. Subsequently, the mixed solution was heated to 100 °C and maintained for 5 h in a constant temperature water bath and then cooled to room temperature. Finally, the ZnO–C_{60} core–shell QDs final product was obtained by using a filter.

2.2.2 *Structural Analysis: X-Ray Diffraction and Transmission Electron Microscopy*

Figure 2.17a shows a high-resolution transmission electron microscopy (HRTEM) image of an individual ZnO–C_{60} core–shell QD. The distorted hexagonal shaped area in the HRTEM image is actually showing C_{60} molecules on ZnO QDs with dimension of a long axis of about 17 nm and short axis of about 12 nm. The Zn–O–C bonding was possibly achieved through the defect like sites created on the acid treated C_{60} oxide and thus the chemical conjugation of C_{60} molecules with

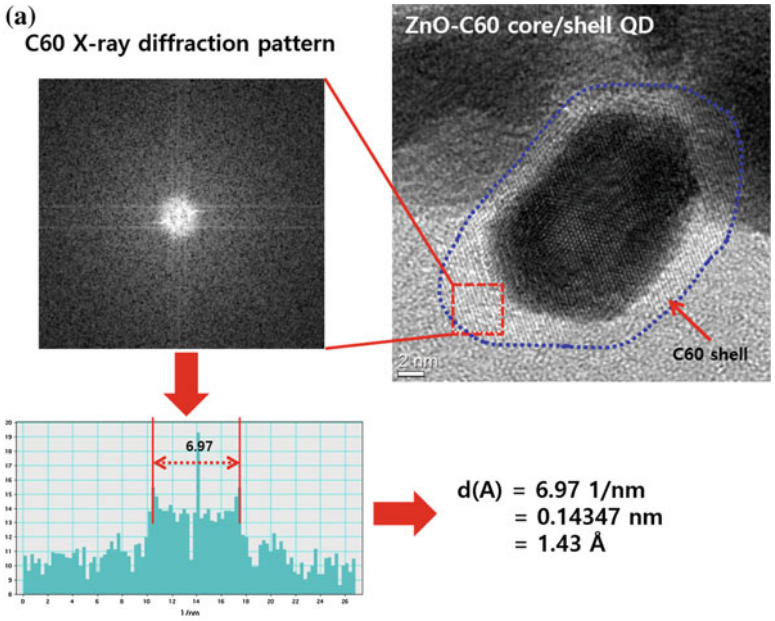
(a)
C60 X-ray diffraction pattern
ZnO-C60 core/shell QD
C60 shell
2nm
6.97
d(A) = 6.97 1/nm
= 0.14347 nm
= 1.43 Å

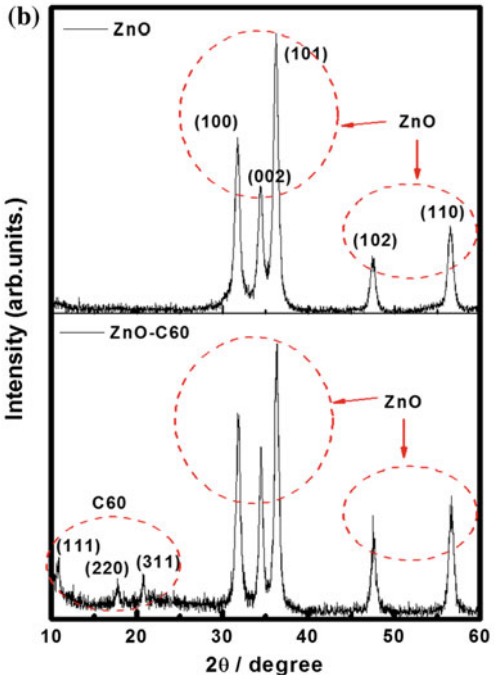
(b)
ZnO
(101)
(100)
(002)
ZnO
(110)
(102)
ZnO-C60
ZnO
C60
(111)
(220)
(311)
Intensity (arb.units.)
10
20
30
40
50
60
2θ / degree

◀ **Fig. 2.17** HRTEM and X-ray diffraction of the synthesized ZnO–C_{60} core–shell QDs. **a** The HRTEM image of the ZnO–C_{60} core–shell QDs. The *red square line* is the image of one ZnO QD covered by C_{60}. The inset shows an enlarged view of C_{60} on the surface of a single ZnO QD. The C–C bond length, although not clearly resolved everywhere, is measured to be 0.14 nm. **b** The appearance of ZnO and C_{60} peaks in XRD patterns gives evidence that the ZnO–C_{60} core–shell QDs include ZnO QDs and C_{60}

ZnO QDs. Further, from HRTEM analysis, the close inspection of the red squared area in the image reveals that the outer shell, encircling the ZnO QDs, is actually composed of C_{60} because a hexagonal atomic lattice with uniform contrast can be clearly observed, and the measured distance between carbon atoms of about 0.14 nm coincides with the theoretical value of C_{60}. As seen in XRD patterns of ZnO–C_{60} core–shell QDs (Fig. 2.17b), simultaneous observation of Bragg peaks of ZnO as well as C_{60} indicates that the consolidated ZnO–C_{60} core–shell QDs were successfully synthesized from C_{60} oxide and zinc acetate dihydrate. The existence of C_{60} on ZnO QDs is confirmed by the appearance of low intensity peaks of (111), (220), and (311) centered at around $2\theta = 10.9°$, 17.74°, and 20.76°, respectively and is in good agreement with the JCPDS (no. 44-0058) data. The ZnO (100), (002), (101), and (102) peaks, without any peaks corresponding to the Zn metal, were also clearly discernible and the position and intensity ratios of these peaks agree well with those of the ZnO bulk (JCPDS no. 36-1451).

2.2.3 Photoluminescence

The (PL) spectrum of ZnO QDs only shows a near-band-edge excitonic emission without a defect-related green band, as shown in Fig. 2.17. The peak at 381 nm (3.25 eV) is matching well with the emission peak observed for the ZnO bulk material (3.25 eV) (Son et al. 2009). On the other hand, the PL peak of ZnO–C_{60} core–shell QDs is greatly reduced (quenched) as indicated by the black line in Fig. 2.17. This result is caused by the conjugation of C_{60} with the ZnO QDs, leads to a PL quenching of about 99.8 % or almost no luminescence. This value is quite larger than ca. 70 % measured in the ZnO–graphene core–shell QDs. In similar way, this can be attributed to an efficient charge separation by direct electron transfer from the ZnO QDs to the C_{60} through a chemical bonding of Zn–O–C. These results confirm the enhanced photo-induced charge transfer in ZnO–C_{60} core–shell QDs. The inset in Fig. 2.18 represents the enlarged PL peak of ZnO–C_{60} core–shell QDs. On the other hand, a new PL peak, not well resolved and not high intensity, can be clearly observed at around 400 nm besides the peak corresponding to ZnO. This can be due to recombination between the transferred electrons on the conduction band (4.3 eV) of C_{60} and holes in the valence band (7.39 eV) of ZnO. The energy of this transition corresponds to about 3.09 eV and is coinciding with the peak observed. It is also noteworthy that, in addition to the large quenching of PL, the intensity of band-to-band transition corresponding to ZnO is lower than that

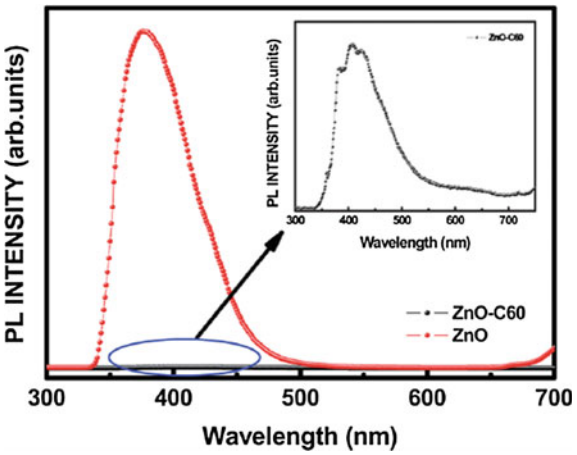

Fig. 2.18 PL spectra of ZnO only QDs (*red line*) and ZnO–C_{60} core–shell QDs (*black line*). The inset shows the magnified PL spectrum of ZnO–C_{60} core–shell QDs (Reproduced from Son et al. 2012a, b, c)

of transition between C_{60} and ZnO, which supports that excited electrons are effectively transferred from ZnO to C_{60}. The QD PL quenching effect may occur by four mechanisms as described in Sect. 2.1.5 (Wang et al. 2008a, b). (1) dynamic quenching, (2) static quenching, (3) quenching by energy transfer, and (4) charge-transfer reactions (Bifeng et al. 2008). In the same way, ZnO QD PL quenching in the presence of C_{60} is proposed to mainly be caused by static quenching and charge-transfer reactions. The other possible way of quenching can be due to the fast deactivation of the excited state by the electron transfer reactions from ZnO to C_{60}. The degree of quenching mainly depends on the number of electrons transferred from the conduction band of ZnO to LUMO levels of C_{60} as well as the duration time on LUMO levels. Blue emission from LUMO levels of C_{60} to the valence band of ZnO mainly consisted of O2p at 3.05 and 2.94 eV (see the inset in Fig. 2.11a, b. Almost complete quenching of all UV and blue emissions in PL indicates that most excited electrons in the conduction band of ZnO were transferred to cathode through high mobility C_{60} before emission from LUMO in C_{60} to the valence band of ZnO occurs. This qualitatively implies a high charge generation efficiency (Beek et al. 2004; Palthi et al. 2010).

2.3 ZnO–Nano Ring Single-Walled CNTs Hybrid Quantum Dots

2.3.1 Synthesis

The pristine single-walled carbon nano tubes (SWCNTs) synthesized by catalyst chemical vapor deposition (CCVD) are purity > 95 wt%, $I_G/I_D > 9$ (Raman data), diameter(1–2 nm), and length ca. ~10 μm (Carbon Nano-Material Technology, Co.) (Fig. 2.19) SWCNTs were chemically functionalized with a mixture of

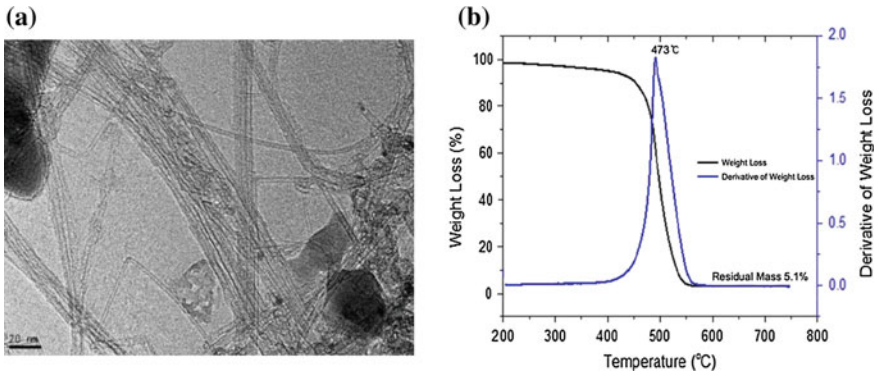

Fig. 2.19 High resolution transmission electron microscope (HRTEM) image (**a**) and TGA data (**b**) of CNTs SP95 (Carbon Nano-Material Technology Co.)

sulfuric and nitric acids (H_2SO_4:HNO_3 = 3:1). And then the SWCNT was reported to be cut into short tubes with most of carboxylic groups (–COOH) covalently attached the sidewalls, defects site, and open ends as illustrated in Fig. 2.20 (Banerjee et al. 2005). The SWCNTs were dispersed in acid mixture by using a multi frequency ultrasonicator. After acid treatment the solution was quenched in cold water, and samples were diluted. Thereafter, the SWCNTs were extracted on a PTFE membrane of 1um pore size using a vacuum filtration assembly. The resulting SWCNTs were dried in an oven at 70 °C for overnight.

In order to synthesize ZnO-NRCNTs nanoparticles, the solution of zinc acetate dehydrate (1.84 g) was prepared in 300 ml dimethylformamide (DMF) under stirring. Acid treated SWCNTs (20 mg) (Fig. 2.21a) were dispersed in 50 ml DMF by using a multi frequency ultrasonicator. The SWCNTs solution was added in the ZnO solution under continuous stirring for 5 h at 150 °C (Fig. 2.21b). The solution was poured into ethanol. After the reaction was quenched, the resulting gray solid products were washed with ethanol and water, centrifuged and then dried in the

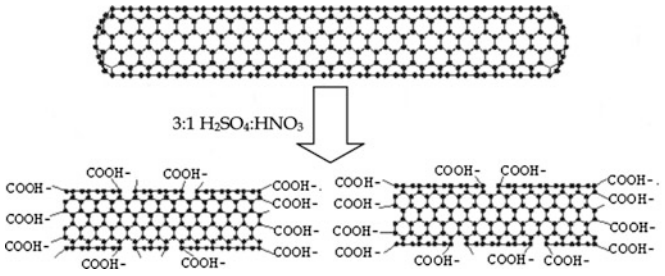

Fig. 2.20 A schematics of the chemical functionalization of a SWCNTs. The SWCNTs are cut into short tubes with carboxylic groups covalently attached the sidewalls and open ends (Reproduced from Banerjee et al. 2005)

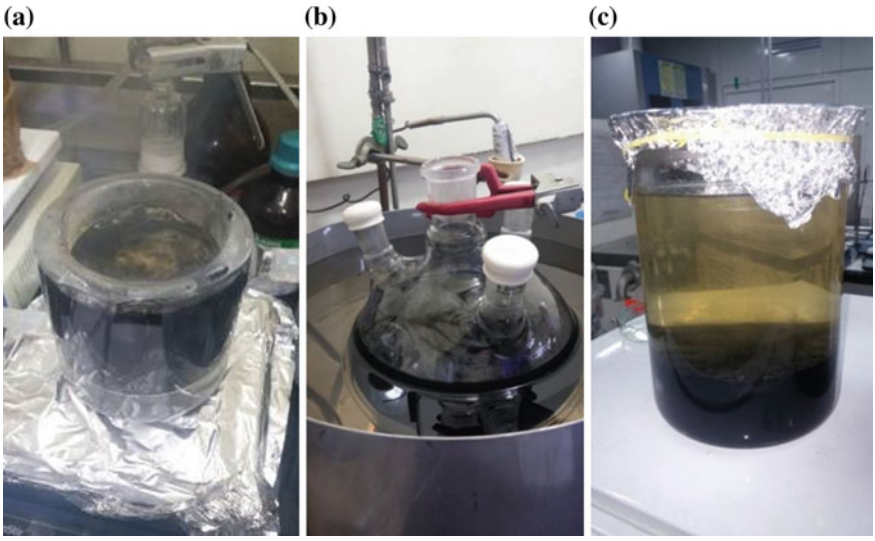

Fig. 2.21 Synthetic process of ZnO–SWCNTs with PVP. **a** Neat CNTs were treated by acid. **b** Acid-treated CNTs was mixed with Zn acetate dehydrate in DMF solution. **c** ZnO–SWCNTs were reacted with PVP for 12 h

vacuum oven for overnight. For ZnO–NRCNTs blend with polyvinylpyrrolidone (PVP) were dissolved in water. In order to NRCNTs binding with PVP, each reagent was blended in solution by using a multi frequency ultrasonicator (Fig. 2.21c). After reaction, for removing unreacted polymer, the solution diluted in water and centrifuged. Resulting product dissolved in hydrochloride acid (HCl) and sonication. After reaction the solution poured into cold ethanol. After the reaction, the NRCNTs were washed with ethanol and water, centrifuged and dried in the vacuum oven for overnight.

2.3.2 Nano-ring SWCNTs (NR-SWCNTs)

Figure 2.22a shows high resolution TEM image of the ZnO-SWCNTs structure. The ZnO inner core is located inside and wrapped by the single-walled CNTs. ZnO is well crystallized as a hexagonal structure with the crystalline spacing of 0.26 nm along with the [002] plane and the long axis of ZnO is estimated to be ca. 10 nm. SWCNTs surround the inner ZnO and the thickness is about 2.5 nm which is equal to the diameter of the two bundle of SWCNTs.

Using HCl, ZnO–SWCNTs are dissolved to remove inner ZnO NPs. And then they were sieved by AAO filter. As shown in Fig. 2.22b, very interesting nano sized and ring shaped SWCNTs, called NR SWCNTs, were obtained. The size of NR SWCNTs is about 20–30 nm and the shape looks like a distorted hexagonal which

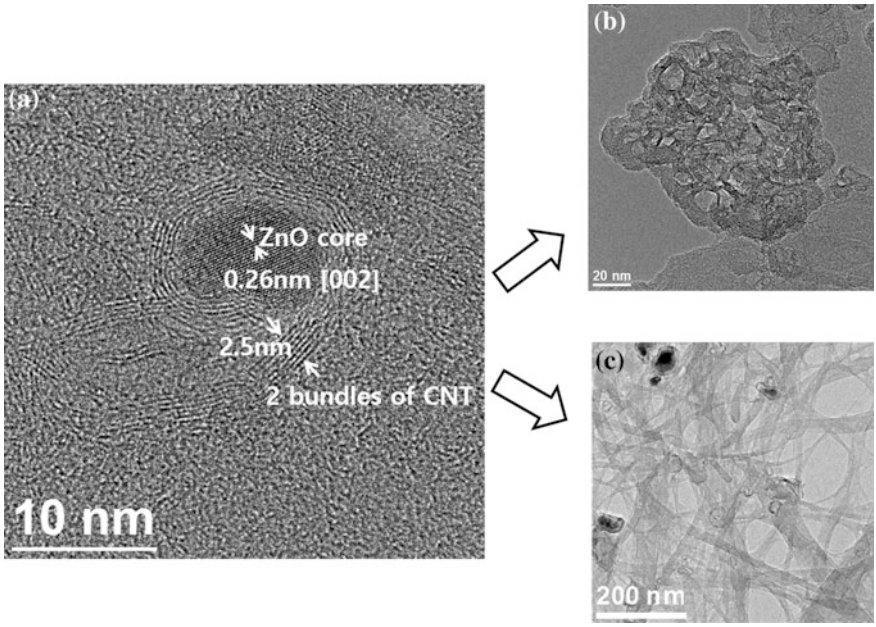

Fig. 2.22 **a** HR TEM images of ZnO–SWCNTs hybrid structure. After dissolving in HCl (inner ZnO was removed), **b** Obtained NR–SWCNTs with AAO filter and **c** sonificated SWCNTs without AAO filter

may be closely related to the crystalline structure of ZnO NPs. There have been some reports on the formation of ring shape CNTs using several approaches such as CVD, sonification or theoretical calculation (Liu et al. 1997; Martel et al.1999; Sano et al. 2001; Colomer et al. 2003; Komatsu et al. 2006; Guo et al. 2007; Geng et al. 2008; Zhang and Li 2009), the formation of nano ring CNTs with a size of smaller than 30 nm has never reported before. During the formation of the ZnO–SWCNTs hybrid structure, mixed phases of both $Zn(OH)_2$ and ZnO as inner cores are simultaneously observed in a reaction time shorter than 1 h and the boundary between ZnO and SWCNTs seems to be simply rounded like circle. But after the reaction time goes past 1 h, $Zn(OH)_2$ turns into ZnO through dehydration and the number of ZnO NPs on the SWCNTs surfaces increases, which leads to the agglomeration and nucleation. In consequence, ZnO NPs (sizes up to 10 nm) crystallizes into hexagonal structure and this cohesion causes SWCNTs to bend and distort locally. After filtering using anodized aluminum oxide (AAO) ceramic filter (with the hole of 100 nm diameter), very uniform These NR–SWCNTs keep the ring shape even after sonification and after two weeks later. It is believed that this solid NR–SWCNTs, called closed NR–SWCNTs, results from the strong chemical bonding of each carboxyl (COOH) groups induced at the edge of open end in cut SWCNTs as shown in Fig. 2.20. Unfortunately the productivity is very low (<4 %) But after ultra sonification without filtering, most of NR-SWCNTs revert to their

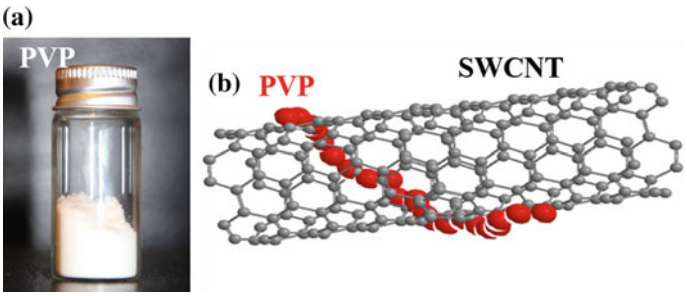

Fig. 2.23 **a** Polyvinylpyrrolidone (PVP; $(C_6H_9NO)_n$) and **b** PVP wrapper bonded with SWCNTs through H-bonding

original linear appearance without maintaining the ring shape as shown in Fig. 2.22c, which implies that a lots of NR-SWCNTs are formed in weak bonding. In order to improve the productivity of NR–SWCNTs, weakly bonded NR–SWCNTs are going to be bound with PVP. It can be easily expected that strong hydrogen bonding between hydroxyl group (–OH) induced SWCNTs and oxygen in PVP$(C_6H_9NO)_n$) and can play a role as a strong wrapper binding between SWCNTs as shown in Fig. 2.23b and keep the ring shape without breaking. By adoption of the PVP wrapper, the productivity of NR-SWCNTs increases up to 98 %.

References

P.O. Anikeeva et al., Nano Lett. **7**, 2196 (2003)
S. Banerjee et al., Adv. Mater. **17**, 17 (2005)
W.J.E. Beek et al., Adv. Mater. **16**, 1009 (2004)
P. Bifeng et al., J. Phys. Chem. C **112**, 939 (2008)
J.F. Colomer et al., Nano Lett. **3**, 685 (2003)
L.J. Cote et al., J. Am. Chem. Soc. **131**, 1043 (2009)
A. Dato et al., Nano Lett. **8**, 2012 (2008)
Z.J. Fan et al., ACS Nano **5**, 191 (2011)
M.G. Frisch et al., *Gaussian 03*, Revision C.02 (2004)
J. Geng et al., J. Phys. Chem. C **112**, 12264 (2008)
A. Guo et al., J. Phys. Chem. C **111**, 3555 (2007)
A.L. Higginbotham et al., ACS Nano **4**, 2059 (2010)
N. Komatsu et al., Carbon **44**, 2089 (2006)
K.N. Kudin et al., Nano Lett. **8**, 36 (2008)
B. Kumar et al., Appl. Phys. Lett. **89**, 071922 (2006)
D. Li et al., Nat. Nanotech. **3**, 101 (2008)
J. Liu et al., Nature **385**, 780 (1997)
J.R. Lomeda et al., J. Am. Chem. Soc. **130**, 16201 (2008)
R. Martel et al., J. Phys. Chem. B **103**, 7551 (1999)
C. Mattevi et al., Adv. Func. Mater. **19**, 2577 (2009)
T.M.G. Mohiuddin et al., Phys. Rev. B **79**, 205433 (2009)
I.K. Moon et al., Nat. Commun. **1**, 1 (2010)

T. Nakajima et al., Carbon **26**, 357 (1988)
Z.H. Ni et al., ACS Nano **2**, 2301 (2008)
A. Palthi et al., J. Macromol. Sci. Part A: Pure Appl. Chem. **47**, 375 (2010)
S. Park et al., Nano Lett. **9**, 1593 (2009)
R.D. Rodriguez et al., Nanoscale Res. Lett. **7**, 682 (2012)
M. Sano et al., Science **293**, 1299 (2001)
D.I. Son et al., Nanotechnology **20**, 195203 (2009)
D.I. Son et al., J. Mater. Chem. **22**, 816 (2012a)
D.I. Son et al., Nat. Nanotechnol. **7**, 465 (2012b)
D.I. Son et al., Nano Res. **5**, 73 (2012c)
L. Tang et al., Adv. Funct. Mater. **19**, 2782 (2009)
G. Wang et al., J. Chem. Phys. **C112**, 8192 (2008a)
F. Wang et al., Science **320**, 206 (2008b)
D. Yang et al., Carbon **47**, 145 (2009)
M. Zhang, J. Li, Materialstoday **12**, 12 (2009)

http://www.springer.com/978-981-10-0979-2

ZnO-Nanocarbon Core-Shell Type Hybrid Quantum Dots

Choi, W.K.

2017, X, 75 p. 55 illus., 47 illus. in color., Softcover
ISBN: 978-981-10-0979-2